Compact optical one-way waveguide isolators for photonic-band-gap microchips

Hiroyuki Takeda and Sajeev John
Department of Physics, University of Toronto, 60 St. George St., Toronto, Ontario, Canada M5S 1A7
(Received 11 June 2008; published 5 August 2008)

In two-dimensional (2D) photonic crystals (PC's), we demonstrate compact optical waveguide isolators in which light can propagate only one way. Waveguides are composed of magneto-optical materials with magnetic domain walls. Magneto-optical effects and magnetic domain walls break time-reversal and space-inversion symmetries, respectively, leading to nonreciprocal waveguides with different group velocities for forward and backward propagating light of a given frequency. When backward light has a zero group velocity, only forward light can be transmitted while backward light stops. Slow leakage of backward light (when the group velocity is not precisely zero) is eliminated by introducing absorption loss in nonreciprocal PC waveguides. Then, absorption of forward light is less than that of backward light. Introducing gain material and signal amplification by current injection, forward light can propagate with no net loss and only backward light is attenuated. We demonstrate that backward light, with nearly zero group velocity, can be eliminated because of absorption over a long effective optical path length. This enables compact on-chip photonic band-gap isolators. The waveguide isolator is assumed to be composed of europium oxide with the Faraday rotation angle of $\theta_F=3.49\times10^3$ rad/cm at wavelength $\lambda=1.5$ μm under a magnetic field 0.9 Tesla. In a waveguide isolator with the length of 8.5 μm, transmittance of backward light is mostly zero at a specific frequency when transmittance of forward light is amplified to 1 by current injection. The usable bandwidth is up to 12 nm centered at 1.5 micron wavelength as the device length is increased ($L=42.6$ μm). We demonstrate similar results for an asymmetric nonreciprocal waveguide without a magnetic domain wall. The possibility of compact on-chip photonic band-gap isolators is demonstrated for 2D membrane photonic crystals with finite thickness in the third dimension. Computations are performed using plane wave expansion, finite difference time domain, and optical Wannier function methods.

DOI: 10.1103/PhysRevA.78.023804 PACS number(s): 42.70.Qs, 42.25.Bs, 78.20.Ls

I. INTRODUCTION

Photonic crystals (PC's) with photonic band gaps (PBG's) are engineered periodic dielectric microstructures in which light can be trapped and cannot propagate in a certain frequency range [1–3]. These complex, three-dimensional, scattering microstructures enable unprecedented forms of optical waveguiding [4–6]. These "semiconductors of light" enable large scale integration of optical components within an optical microchip. PC's enable unconventional guiding of light in air waveguides and dense integration of microscopic optical components, into an optical microchip [4,7–11]. In conventional optical circuits, diffraction and scattering losses may become prohibitive at sharp waveguide bends and in the presence of surface roughness. The PBG, on the other hand, eliminates such leakages of light at a fundamental level.

On the other hand, optical isolators in which light can propagate only one-way play a crucial role in integrated optics. For example, reflection from nearby structures of emitted light can make the operation of laser diodes unstable. For dense integration of optical components on a photonic band-gap microchip, it is important that light propagating along a long circuit path does not result in a large scale optical interference pattern. In such an interference pattern, small modifications of light amplitude in one part of the optical circuit can trigger unwanted large changes in optical amplitude in a remote part of the circuit. For conventional optical isolators, Faraday effects in magneto-optical materials are used [12] to eliminate unwanted feedback: Incident light is polarized in the x direction using a polarizer at $z=0$. A magneto-optical material is placed in the interval $0\leqslant z\leqslant L$ and magnetized in the z direction. When the light propagates from $z=0$ to $z=L$, the polarization of transmitted light rotates by 45°. Moreover when reflected light propagates from $z=L$ to $z=0$, the polarization of the reflected light rotates by 45° in the opposite sense. In other words, a total rotation angle of the polarization of the light returning to $z=0$ is 90° and is eliminated by the polarizer.

In the study of optical circuits, optical waveguide isolators without polarizers are attempted [13–15]. In conventional waveguides, frequencies are symmetric with respect to wave vectors, $\omega_{n\mathbf{k}}=\omega_{n-\mathbf{k}}$, where ω, n, and $\mathbf{k}$ are the angular frequency, the photonic band number, and the wave vector, respectively. Then, absolute values of wave vectors $\mathbf{k}^{(f)}$ of forward and $\mathbf{k}^{(b)}$ backward light are the same, $|\mathbf{k}^{(f)}|=|\mathbf{k}^{(b)}|$ ($\mathbf{k}^{(b)}=-\mathbf{k}^{(f)}$). However, in waveguides with magnetic domain walls magnetized in the opposite directions, unconventional optical properties are obtained. Magneto-optical effects and magnetic domain walls break time-reversal and space-inversion symmetries, respectively. Both time-reversal and space-inversion symmetry breakings enable nonreciprocal waveguides, $\omega_{n\mathbf{k}}\neq\omega_{n-\mathbf{k}}$. Then, absolute values of wave vectors of forward and backward light are different, $|\mathbf{k}^{(f)}|\neq|\mathbf{k}^{(b)}|$. Details of this nonreciprocity are discussed in the Appendix.

Optical waveguide isolators using the above nonreciprocity have been studied previously [13–15]. For example, an isolator can be constructed using parallel reciprocal and nonreciprocal waveguides. While in the reciprocal waveguide $|\mathbf{k}^{(f)}|=|\mathbf{k}^{(b)}|=k_0$, in the nonreciprocal waveguide $|\mathbf{k}^{(f)}|=k_1\neq k_0$ and $|\mathbf{k}^{(b)}|=k_0$. Forward light in the reciprocal waveguide cannot couple to the nonreciprocal waveguide because wave vectors of forward light are different in these waveguides and forward light propagates only along the reciprocal wave-

guide. On the other hand, backward light in the reciprocal waveguide couples to the nonreciprocal waveguide because wave vectors of backward light are the same in these waveguides. In this manner, backward light is eliminated from the reciprocal waveguide.

Optical waveguide isolators using Mach-Zehnder interferometers have also been reported [16,17]. Recently, an application of optical waveguide isolators to PC's has been proposed [18]. Optical circulators in Y-shaped PC waveguides with a point defect composed of magneto-optical materials have also been reported [19,20]. However, these optical waveguide isolators are relatively large and need to couple several waveguides to eliminate backward light. It is preferable to design a more compact optical waveguide isolator in a single waveguide.

In electronics, there is an effect called the "quantum Hall edge state" in which electrons flow only one way [21]. An application of the quantum Hall edge state to PC's has been proposed by Haldane and Raghu [22,23]: In two-dimensional (2D) triangular-lattice PC's there appears a twofold degenerate frequency called the "Dirac point" with a linear dispersion relation near the corresponding K point in the first Brillouin zone. This twofold degeneracy can be lifted by magneto-optical effects, and a new PBG appears. Using magnetic domain walls as interfaces, the analogy of quantum Hall edge states, in which light propagates only one way, can be obtained along the domain wall. This occurs in a frequency region of the new PBG. We have demonstrated this mechanism in 2D square-lattice PC's and obtained one-way waveguides in numerical simulations [24]. However, the integration of such an "edge state," one-way waveguide into a photonic circuit, destroys the functionality of this type of optical isolator. When an interface or boundary is formed between the "edge state" isolator and the remainder of the (nonmagnetic) photonic chip, light leaks backward along the boundary. In analogy to the quantum Hall edge states, light simply circulates around the edges of the magnetic region of the chip and optical isolator functionality is lost. Therefore, we consider an alternative mechanism.

In nonreciprocal waveguides, group velocities of forward and backward light are different. However, the difference of the group velocities is generally small, even if a large magneto optical effect is employed. On the other hand, PC waveguides can exhibit strongly varying optical dispersion in different regions of **k** space. The group velocity of light is given by the gradient of the waveguide dispersion relations. An alternative paradigm for optical isolator functionality consists of a nonreciprocal waveguide with high group velocity in the forward direction, but nearly vanishing group velocity in the backward direction, over a fixed frequency band. This means only forward light can propagate, whereas backward light stops. It has been reported that in one-dimensional (1D) stacked layers composed of giant anisotropic and magneto-optical materials, backward light with a zero group velocity can be obtained [25].

In this paper, we consider a nonreciprocal PC waveguide in which a group velocity of backward light is zero. We use nonreciprocal waveguides composed of magneto-optical materials with magnetic domain walls in 2D triangular-lattice PC's composed of air holes in a Si substrate. In practice, however, there is a slow leakage of backward light because the group velocity is not zero completely. To eliminate this leakage of backward light, we introduce absorption in the nonreciprocal PC waveguide. In this case, absorption of forward light is smaller than that of backward light [26]. The absorption of forward light can be compensated through gain provided by current injection. Then, forward light can propagate without attenuation and only backward light decays (despite reduced absorption due to current injection).

The critical issues for on-chip integration of an optical isolator are (i) the contrast between forward and backward transmitted light intensity, (ii) the frequency bandwidth over which effective nonreciprocity is achieved, and (iii) the overall size of the optical isolation device. In conventional architectures, absorption of backward light is small, and so a long waveguide is required to eliminate the backward light. However, absorption is enhanced greatly in backward light with nearly zero group velocity. This enables compact on-chip PBG isolators. We also demonstrate efficient coupling of reciprocal and nonreciprocal waveguides. Our isolator architecture consists of a central nonreciprocal waveguide with absorption, connected to reciprocal waveguide ports on either end. We investigate transmittance and reflectance of forward and backward light in the coupling of the reciprocal and nonreciprocal waveguides. The waveguide isolator is assumed to be composed of EuO with the Faraday rotation angle $\theta_F = 3.49 \times 10^3$ rad/cm at wavelength $\lambda = 1.5$ μm under a magnetic field 0.9 Tesla. In a waveguide isolator of the length 8.5 μm, transmittance of backward light is mostly zero when transmittance of forward light is amplified to 1 by current injection. This enables compact on-chip photonic band-gap isolators. The usable bandwidth is up to 12 nm centered at 1.5 micron wavelength in a waveguide isolator of the length 42.6 μm. We also demonstrate similar functionality in an asymmetric nonreciprocal waveguide without a magnetic domain wall. Finally, we demonstrate compact on-chip PBG isolators in 2D membrane PC's.

This paper is organized as follows. In Sec. II, we introduce the structures of waveguides, absorption of forward and backward light, and coupling of reciprocal and nonreciprocal waveguides. In Sec. III, we describe the computational methods of the plane wave expansion (PWE) method, finite-difference time-domain (FDTD) method, and Wannier function (WF) method. In Sec. IV, we present numerical results and their interpretation. Finally, in Sec. V we present our conclusions.

II. MODEL SYSTEMS

A. Waveguide architecture

When magneto-optical materials are magnetized in the z direction, two kinds of light propagation can be considered: One is the light propagation parallel to the magnetization (Faraday configuration), and the other is the light propagation perpendicular to the magnetization (Voigt configuration). In the Faraday configuration, a polarization of light rotates in the same directions, regardless of the propagation in the positive or negative z direction. Magnitudes of rotations per unit length are defined by the Faraday rotation

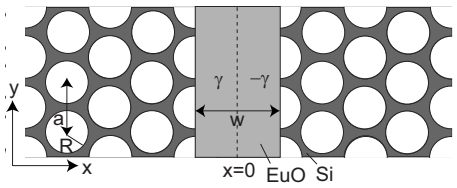

FIG. 1. Structure of a nonreciprocal waveguide in a 2D triangular-lattice PC composed of air holes in a Si substrate. Dark and light shaded regions indicate Si and EuO, respectively. Dielectric constants of Si and EuO are $\epsilon=11.9$ and $\epsilon=6.0$, respectively. A radius of an air hole is $R/a=0.43$, and the width of the waveguide is $w=\sqrt{3}a$, where a is the lattice constant. At $x=0$, there is a magnetic domain wall drawn by a dashed line. For $-\sqrt{3}/2<x/a<0$ and $0<x/a<\sqrt{3}/2$, $\gamma(\mathbf{r})=\gamma$ and $\gamma(\mathbf{r})=-\gamma$, respectively, in Eq. (1). Otherwise, $\gamma(\mathbf{r})=0$.

angle θ_F, proportional to magnitudes of external magnetic fields. The Faraday configuration is widely used for optical isolators, as described in Sec. I. While in the Faraday configuration polarizations of light rotate, in the Voigt configuration polarizations do not change. In a PBG microchip, the polarization of light is fixed within a waveguide. For our on-chip optical waveguide isolators, therefore, we consider the Voigt configuration in which electric field of light is in the 2D xy plane [transverse electric (TE) mode].

In magneto-optical materials magnetized in the z direction, we consider the dielectric tensor

$$\boldsymbol{\epsilon}(\mathbf{r})=\begin{bmatrix}\epsilon_{xx}(\mathbf{r}) & \epsilon_{xy}(\mathbf{r}) & 0\\ \epsilon_{yx}(\mathbf{r}) & \epsilon_{yy}(\mathbf{r}) & 0\\ 0 & 0 & \epsilon_{zz}(\mathbf{r})\end{bmatrix}=\begin{bmatrix}\epsilon(\mathbf{r}) & -i\gamma(\mathbf{r}) & 0\\ i\gamma(\mathbf{r}) & \epsilon(\mathbf{r}) & 0\\ 0 & 0 & \epsilon(\mathbf{r})\end{bmatrix}. \tag{1}$$

When $\epsilon(\mathbf{r})$ and $\gamma(\mathbf{r})$ are real, there is no absorption. $\gamma(\mathbf{r})$ determines the Faraday rotation angle. In PC's, the dielectric tensor is periodic $\boldsymbol{\epsilon}(\mathbf{r})=\boldsymbol{\epsilon}(\mathbf{r}+\mathbf{R})$, where $\mathbf{R}$ is the lattice vector. Nonreciprocal PC waveguides are composed of magneto-optical materials with magnetic domain walls magnetized in the opposite directions [rapid change in sign of $\gamma(\mathbf{r})$ along a fixed line].

A large PBG is required to obtain effective guided modes in which light is strongly localized in the waveguide. 2D triangular-lattice PC's composed of circular air holes and 2D square-lattice PC's composed of square air holes have large PBG's for TE modes. Since it is easier to experimentally fabricate circular air holes than square air holes, we use the 2D triangular-lattice PC's. In Fig. 1, we show the structure of a nonreciprocal waveguide in a 2D triangular-lattice PC composed of air holes in a Si substrate. Dark and light shaded regions indicate Si and europium oxide (EuO), respectively. The nonreciprocal waveguide is composed of EuO. This material has larger Faraday rotation angles than conventional magneto-optical materials such as garnets, as described in Sec. IV. Dielectric constants of Si and EuO are $\epsilon=11.9$ and $\epsilon=6.0$, respectively. The radius of each air hole is $R/a=0.43$, and the width of the waveguide is $w=\sqrt{3}a$, where a is the lattice constant. The waveguide is parallel to the y axis. At $x=0$, there is a magnetic domain wall drawn by a dotted line. For $-\sqrt{3}/2<x/a<0$, $\gamma(\mathbf{r})=\gamma$ and for $0<x/a<\sqrt{3}/2$, $\gamma(\mathbf{r})=-\gamma$, in Eq. (1). Otherwise, $\gamma(\mathbf{r})=0$. A physical geometry for applying magnetic fields is discussed in Sec. IV. This waveguide is nonreciprocal, and group velocities of forward and backward light are different. As described below, at a certain band of frequencies, backward light nearly stops because of near vanishing group velocity. This means that only forward light can propagate. In practice, however, there is slow leakage of backward light in the absence of absorption.

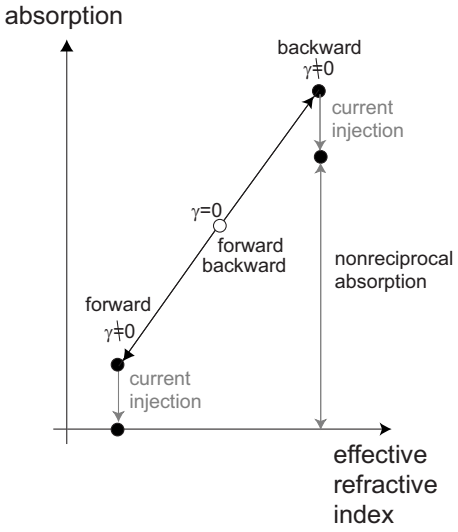

FIG. 2. Schematic model of nonreciprocal absorption in forward and backward light. Horizontal and vertical axes indicate the effective refractive index (optical path length) and absorption, respectively. White and black points indicate absorption of $\gamma=0$ and $\gamma\neq 0$, respectively. Gray arrows indicate the gains of current injection. To amplify the same amount for forward and backward light, the current injection should be conducted outside the nonreciprocal waveguide.

B. Absorption of forward and backward light

To eliminate the leakage of backward light, we consider absorption in the nonreciprocal waveguide. Figure 2 shows a schematic model of nonreciprocal absorption in forward and backward light. Horizontal and vertical axes indicate the effective refractive index (optical path length) and absorption, respectively. When $\gamma=0$, absorption described by the open white circle is the same for forward and backward light. When $\gamma\neq 0$, absorption described by solid circles is smaller for forward light than for backward light [26]. The smaller absorption of forward light is then compensated through gain provided by current injection (gray arrows) [26]. In this manner, the net loss of forward light artificially becomes zero. Absorption of backward light is also reduced but the net loss is nonzero. Consequently, forward light propagates without overall loss and only backward light is attenuated. Electrodes for current injection are placed at the top (z direction) of the waveguide arranged in the xy plane [26]. Absorption is enhanced greatly if backward light exhibits a zero group velocity. Even for a short waveguide segment, backward light ex-

periences a very long effective path length. This enables a compact optical waveguide isolator.

When introducing active materials into waveguides or metallic electrodes adjacent to the waveguides, an imaginary part ϵ_i appears in the dielectric constant $\epsilon=6.0+i\epsilon_i$. In the case of $\gamma=0$, absorption is the same in forward and backward light. In the case of $\gamma\neq 0$, however, absorption can be different for forward versus backward light. In the optical Bloch functions, the wave vectors of forward and backward light are modified slightly by a small ϵ_i. This change of wave vector for a fixed frequency is given by

$$\delta k_y = \frac{\partial k_y}{\partial \epsilon}(i\epsilon_i) = -i\left(\frac{\partial \omega}{\partial \epsilon}\Big/\frac{\partial \omega}{\partial k_y}\right)\epsilon_i. \tag{2}$$

In Eq. (2), we use the condition that the operational frequency is held constant: $d\omega=(\partial\omega/\partial\epsilon)d\epsilon+(\partial\omega/\partial k_y)dk_y=0$. As group velocity $\partial\omega/\partial k_y$ becomes smaller, $|\delta k_y|$ becomes larger. As shown later, by band-structure calculation, $\partial k_y^{(f)}/\partial\epsilon>0$ and $\partial k_y^{(b)}/\partial\epsilon<0$ in forward and backward light, respectively. ϵ_i is chosen positive for the case of absorption.

We consider a nonreciprocal waveguide with absorption for $0\leqslant y\leqslant L$. While the forward light is injected at $y=0$ and transmitted at $y=L$, the backward light enters $y=L$ and exits at $y=0$. It follows that for forward light $e^{i(k_y^{(f)}+\delta k_y^{(f)})y}=e^{ik_y^{(f)}y}e^{-|\delta k_y^{(f)}|y}$, whereas for backward light $e^{i(k_y^{(b)}+\delta k_y^{(b)})(y-L)}=e^{ik_y^{(b)}(y-L)}e^{|\delta k_y^{(b)}|(y-L)}$. We assume that the group velocity for backward light is made much smaller than for forward light by magneto-optical effects and that $|\delta k_y^{(f)}|<|\delta k_y^{(b)}|$. Absorption causes decays in both forward and backward light. However, absorption of the forward light can be compensated by current injection, as shown in Fig. 2. At the two exit ports, absolute values of forward and backward optical Bloch functions are $e^{-|\delta k_y^{(f)}|L}$ and $e^{-|\delta k_y^{(b)}|L}$, respectively. We assume that forward and backward light are amplified outside the nonreciprocal waveguide. Then, the same amplification, $e^{|\delta k_y^{(f)}|L}$, is applied to both forward and backward light. In the end, the absolute values of forward and backward optical Bloch functions become 1 and $e^{-(|\delta k_y^{(b)}|-|\delta k_y^{(f)}|)L}$, respectively.

C. Coupling of reciprocal and nonreciprocal waveguides

In Fig. 3, we depict the integration of a nonreciprocal waveguide into an otherwise reciprocal waveguide circuit. In the left and right regions there are reciprocal waveguides without absorption, and in a central region there is an active nonreciprocal waveguide with absorption. Nanomagnets placed above and below the "nonreciprocal waveguide," and electrodes for current injection are placed above and below the waveguide in the "reciprocal region" where forward light is input. We take $\epsilon_D=6.15$ and $\gamma=0.0$ as a dielectric constant of the reciprocal waveguides. The length of the nonreciprocal waveguide is $L/a=20$. We investigate transmittance and reflectance of forward and backward light in the coupling of the reciprocal and nonreciprocal waveguides. While the forward light is injected at $y=0$ in the positive y direction, the backward light is injected at $y=L$ in the negative y direction.

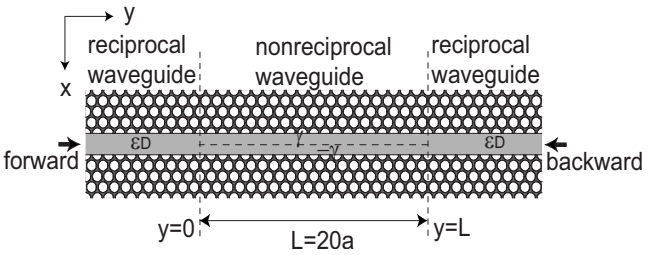

FIG. 3. Coupling of reciprocal and nonreciprocal waveguides to form on-chip optical isolator. In left and right regions there are reciprocal waveguides without absorption, and in a central region there is a nonreciprocal waveguide with absorption. We take $\epsilon_D=6.15$ and $\gamma=0.0$ as the dielectric constant of the reciprocal waveguides. The length of the nonreciprocal waveguide is $L/a=20$. While the forward light enters in the positive y direction, the backward light enters in the negative y direction. Nanomagnets placed above and below the "nonreciprocal waveguide," and electrodes for current injection are placed above and below the waveguide in the "reciprocal region" where forward light is input.

III. COMPUTATIONAL METHODS

A. Plane wave expansion method

For calculations of guided modes in waveguides, we use the PWE method. We consider the magnetic-field Maxwell wave equation with time dependence $e^{-i\omega_{n\mathbf{k}}t}$,

$$\nabla\times[\boldsymbol{\epsilon}^{-1}(\mathbf{r})\cdot\nabla\times\mathbf{H}_{n\mathbf{k}}(\mathbf{r})]=\frac{\omega_{n\mathbf{k}}^2}{c^2}\mathbf{H}_{n\mathbf{k}}(\mathbf{r}), \tag{3}$$

where n and $\mathbf{k}$ indicate the photonic band index and the wave vector, respectively. A Bloch function of the magnetic field is expressed as

$$\mathbf{H}_{n\mathbf{k}}(\mathbf{r})=\mathbf{h}_{n\mathbf{k}}(\mathbf{r})e^{i\mathbf{k}\cdot\mathbf{r}}, \tag{4}$$

and the periodic part of the Bloch function is defined as

$$\mathbf{h}_{n\mathbf{k}}(\mathbf{r})=\sum_{\mathbf{G}}\mathbf{h}_{n\mathbf{k}}(\mathbf{G})e^{i\mathbf{G}\cdot\mathbf{r}}=\sum_{\mathbf{G}}\sum_{\lambda=1,2}h_{n\mathbf{k}}^{\lambda}(\mathbf{G})\mathbf{e}_{\mathbf{k}+\mathbf{G}}^{\lambda}e^{i\mathbf{G}\cdot\mathbf{r}}, \tag{5}$$

where $\mathbf{G}$ is the reciprocal lattice vector. $\mathbf{e}_{\mathbf{k}+\mathbf{G}}^{\lambda=1,2}$ are polarization vectors orthogonal to $\mathbf{k}+\mathbf{G}$.

By substituting $\boldsymbol{\epsilon}(\mathbf{r})=\Sigma_{\mathbf{G}}\boldsymbol{\epsilon}(\mathbf{G})e^{i\mathbf{G}\cdot\mathbf{r}}$ and the Bloch function into Eq. (3), we obtain the eigenvalue matrix equation

$$\sum_{\mathbf{G}'}|\mathbf{k}+\mathbf{G}||\mathbf{k}+\mathbf{G}'|\begin{bmatrix}\mathbf{e}_{\mathbf{k}+\mathbf{G}}^2\cdot\boldsymbol{\epsilon}^{-1}(\mathbf{G}-\mathbf{G}')\cdot\mathbf{e}_{\mathbf{k}+\mathbf{G}'}^2 & -\mathbf{e}_{\mathbf{k}+\mathbf{G}}^2\cdot\boldsymbol{\epsilon}^{-1}(\mathbf{G}-\mathbf{G}')\cdot\mathbf{e}_{\mathbf{k}+\mathbf{G}'}^1\\ -\mathbf{e}_{\mathbf{k}+\mathbf{G}}^1\cdot\boldsymbol{\epsilon}^{-1}(\mathbf{G}-\mathbf{G}')\cdot\mathbf{e}_{\mathbf{k}+\mathbf{G}'}^2 & \mathbf{e}_{\mathbf{k}+\mathbf{G}}^1\cdot\boldsymbol{\epsilon}^{-1}(\mathbf{G}-\mathbf{G}')\cdot\mathbf{e}_{\mathbf{k}+\mathbf{G}'}^1\end{bmatrix}\begin{bmatrix}h_{n\mathbf{k}}^1(\mathbf{G}')\\ h_{n\mathbf{k}}^2(\mathbf{G}')\end{bmatrix}=\frac{\omega_{n\mathbf{k}}^2}{c^2}\begin{bmatrix}h_{n\mathbf{k}}^1(\mathbf{G})\\ h_{n\mathbf{k}}^2(\mathbf{G})\end{bmatrix}. \tag{6}$$

Here, $\boldsymbol{\epsilon}^{-1}(\mathbf{G}-\mathbf{G}')$ is the $(\mathbf{G},\mathbf{G}')$ element of the inverse of the matrix $\boldsymbol{\epsilon}(\mathbf{G}-\mathbf{G}')$ [27,28]. When the number of reciprocal lattice vectors is N_G, the dimension of the matrices $\boldsymbol{\epsilon}(\mathbf{G}-\mathbf{G}')$ and $\boldsymbol{\epsilon}^{-1}(\mathbf{G}-\mathbf{G}')$ is $3N_G$. As discussed later, this full eigenvalue matrix equation is used for 2D membrane PC's.

In an idealization of 2D PC's (with no third dimension), we define $\mathbf{k}+\mathbf{G}=(k_x+G_x,k_y+G_y,0)$, $\mathbf{e}^1_{\mathbf{k}+\mathbf{G}}=(0,0,1)$ and $\mathbf{e}^2_{\mathbf{k}+\mathbf{G}}=(k_y+G_y,-(k_x+G_x),0)/|\mathbf{k}+\mathbf{G}|$. Since off-diagonal terms in Eq. (6) become zero in this idealization, we decompose the wave equation into two independent matrix eigenvalue equations,

$$\sum_{\mathbf{G}'} H^{TE}_{\mathbf{k}}(\mathbf{G},\mathbf{G}')h^1_{n\mathbf{k}}(\mathbf{G}') = \frac{\omega^2_{n\mathbf{k}}}{c^2}h^1_{n\mathbf{k}}(\mathbf{G}) \tag{7}$$

and

$$\sum_{\mathbf{G}'} H^{TM}_{\mathbf{k}}(\mathbf{G},\mathbf{G}')h^2_{n\mathbf{k}}(\mathbf{G}') = \frac{\omega^2_{n\mathbf{k}}}{c^2}h^2_{n\mathbf{k}}(\mathbf{G}), \tag{8}$$

where

$$\begin{aligned} H^{TE}_{\mathbf{k}}(\mathbf{G},\mathbf{G}') = {} & \epsilon^{-1}_{xx}(\mathbf{G}-\mathbf{G}')(k_y+G_y)(k_y+G'_y) \\ & + \epsilon^{-1}_{yy}(\mathbf{G}-\mathbf{G}')(k_x+G_x)(k_x+G'_x) \\ & - \epsilon^{-1}_{xy}(\mathbf{G}-\mathbf{G}')(k_y+G_y)(k_x+G'_x) \\ & - \epsilon^{-1}_{yx}(\mathbf{G}-\mathbf{G}')(k_x+G_x)(k_y+G'_y) \end{aligned} \tag{9}$$

and

$$H^{TM}_{\mathbf{k}}(\mathbf{G},\mathbf{G}') = \epsilon^{-1}_{zz}(\mathbf{G}-\mathbf{G}')|\mathbf{k}+\mathbf{G}||\mathbf{k}+\mathbf{G}'|. \tag{10}$$

Equations (7) and (8) are eigvenvalue matrix equations in the TE and transverse magnetic (TM) modes, respectively. In the TE mode, the electric field is always in the xy plane whereas the magnetic field is in z direction. In the TM mode, the electric field is parallel to the z direction and the magnetic field is always in the xy plane. Magneto-optical materials magnetized in the z direction [Eq. (1)], affect only the TE mode because $\epsilon^{-1}_{zz}(\mathbf{G}-\mathbf{G}')$ in Eq. (10) does not depend on γ, as shown in Eq. (1). We consider 2D triangular-lattice PC's with large TE PBG's composed of air holes in dielectric substrates.

B. Finite-difference time-domain method

For calculations of light propagation in nonreciprocal PC waveguides, we use the FDTD method [29]. We consider real $\epsilon(\mathbf{r})$ and $\gamma(\mathbf{r})$ in Eq. (1). Frequency-dependent electromagnetic fields $\mathbf{E}(\mathbf{r},\omega)$ and $\mathbf{H}(\mathbf{r},\omega)$ with the dielectric tensor in Eq. (1) satisfy the following Maxwell equations (in MKS units):

$$\nabla\times\mathbf{E}(\mathbf{r},\omega) = i\omega\mu_0\mathbf{H}(\mathbf{r},\omega), \tag{11}$$

$$\begin{aligned} \nabla\times\mathbf{H}(\mathbf{r},\omega) = {} & \begin{bmatrix} 0 & -\omega\epsilon_0\gamma(\mathbf{r}) & 0 \\ \omega\epsilon_0\gamma(\mathbf{r}) & 0 & 0 \\ 0 & 0 & 0 \end{bmatrix}\mathbf{E}(\mathbf{r},\omega) \\ & - i\omega\epsilon_0\epsilon(\mathbf{r})\mathbf{E}(\mathbf{r},\omega), \end{aligned} \tag{12}$$

where ϵ_0 and μ_0 are the permittivity and permeability in vacuum, respectively. Using a monochromatic point source of frequency ω_{in} placed outside the waveguide, we consider time-dependent electromagnetic fields $\mathbf{E}(\mathbf{r},t)$ and $\mathbf{H}(\mathbf{r},t)$. For computational simplicity, we change $-i\omega$ to $\partial/\partial t$ on the right-hand side of Eq. (11), we fix $\omega=\omega_{in}$ in the first term on the right-hand side of Eq. (12), and we change $-i\omega$ to $\partial/\partial t$ in the second term. This yields

$$\nabla\times\mathbf{E}(\mathbf{r},t) = -\mu_0\frac{\partial\mathbf{H}(\mathbf{r},t)}{\partial t}, \tag{13}$$

$$\nabla\times\mathbf{H}(\mathbf{r},t) = \boldsymbol{\sigma}(\mathbf{r})\cdot\mathbf{E}(\mathbf{r},t) + \epsilon_0\epsilon(\mathbf{r})\frac{\partial\mathbf{E}(\mathbf{r},t)}{\partial t}, \tag{14}$$

where

$$\boldsymbol{\sigma}(\mathbf{r}) = \begin{bmatrix} 0 & -\omega_{in}\epsilon_0\gamma(\mathbf{r}) & 0 \\ \omega_{in}\epsilon_0\gamma(\mathbf{r}) & 0 & 0 \\ 0 & 0 & 0 \end{bmatrix}. \tag{15}$$

In this formulation, all parameters are real. It is assumed that quasimonochromatic fields have $\Delta\omega/\omega_{in}\ll 1$, where ω_{in} is the center frequency of the pulse and $\Delta\omega$ is the spectral width. In the FDTD method, we discretize Eqs. (13) and (14) with respect to time and space [29]. We take $\Delta x/a=\Delta y/a=0.01$ and $c\Delta t/a=0.005$ as discretizations of time and space.

C. Wannier function method

The FDTD method described above requires very fine discretizations and a large computational domain. This occurs because, unlike conventional PC waveguides, our optical isolator involves backward light propagation with nearly zero group velocity. This requires very long computational time. The WF method is much more efficient under these circumstances [30–32].

In the WF method, we consider the electric-field Maxwell wave equation

$$\nabla\times\nabla\times\mathbf{E}(\mathbf{r}) = \frac{\omega^2}{c^2}[\epsilon_p(\mathbf{r}) + \delta\boldsymbol{\epsilon}(\mathbf{r})]\mathbf{E}(\mathbf{r}), \tag{16}$$

where $\epsilon_p(\mathbf{r})$ is the periodic dielectric constant [$\epsilon=6.0$ and $\gamma=0$ in the waveguide (see Fig. 1)], and $\delta\boldsymbol{\epsilon}(\mathbf{r})$ is the defect dielectric tensor describing magneto-optical effects. We expand electric fields in the basis of maximally localized WF's $\mathbf{W}_{n\mathbf{R}}(\mathbf{r})$ obtained in the absence of $\delta\boldsymbol{\epsilon}(\mathbf{r})$,

$$\mathbf{E}(\mathbf{r}) = \sum_{n\mathbf{R}} E_{n\mathbf{R}}\mathbf{W}_{n\mathbf{R}}(\mathbf{r}), \tag{17}$$

where n and $\mathbf{R}$ are the photonic band number and the lattice vector, respectively. $E_{n\mathbf{R}}$ is the expansion coefficient. $\mathbf{W}_{n\mathbf{R}}(\mathbf{r})$ can be chosen real and are localized near $\mathbf{R}$. The WF's have the following relations, $\nabla\cdot\{\epsilon_p\mathbf{W}_{n\mathbf{R}}\}=0$ and $\langle\mathbf{W}_{n\mathbf{R}}|\epsilon_p|\mathbf{W}_{n'\mathbf{R}'}\rangle=\delta_{nn'}\delta_{\mathbf{R}\mathbf{R}'}$. By substituting Eq. (17) into Eq. (16) and using the orthogonality indicated above, we obtain the matrix equation

$$\sum_{n'\mathbf{R}'} A^{nn'}_{\mathbf{RR}'} E_{n'\mathbf{R}'} = \frac{\omega^2}{c^2} \sum_{n'\mathbf{R}'} \{\delta_{nn'}\delta_{\mathbf{RR}'} + D^{nn'}_{\mathbf{RR}'}\} E_{n'\mathbf{R}'}, \quad (18)$$

where

$$A^{nn'}_{\mathbf{RR}'} \equiv \langle \mathbf{W}_{n\mathbf{R}} | \nabla \times \nabla \times | \mathbf{W}_{n'\mathbf{R}'} \rangle \quad (19)$$

and

$$D^{nn'}_{\mathbf{RR}'} \equiv \langle \mathbf{W}_{n\mathbf{R}} | \delta\boldsymbol{\epsilon} | \mathbf{W}_{n'\mathbf{R}'} \rangle. \quad (20)$$

The divergence condition, $\nabla \cdot \{\boldsymbol{\epsilon}_p + \delta\boldsymbol{\epsilon}\}\mathbf{E} = 0$, is weakly violated by our choice of $\nabla \cdot \{\boldsymbol{\epsilon}_p \mathbf{W}_{n\mathbf{R}}\} = 0$. However, the resulting error is negligible since $\delta\boldsymbol{\epsilon}$ is much smaller than $\boldsymbol{\epsilon}_p$. When using maximally localized WF's, $A^{nn'}_{\mathbf{RR}'}$ and $D^{nn'}_{\mathbf{RR}'}$ decay rapidly with increasing $|\mathbf{R} - \mathbf{R}'|$. The resulting sparse matrix equation enables rapid calculation. We use this matrix equation to calculate waveguide modes and transmission and reflection [30–32] from the optical isolator. The WF method reduces computational time relative to the FDTD method by roughly two orders of magnitude.

IV. NUMERICAL RESULTS AND DISCUSSION

A. Magneto-optical parameters

In order to realize a compact (<10 micron length) on-chip optical isolator, a large magneto-optical effect is required. In thin-film bismuth iron garnet (BIG) at room temperature, the Faraday rotation angle is $\theta_F = 1.36 \times 10^3$ rad/cm at wavelength $\lambda = 635$ nm under a magnetic field 0.3 Tesla [33]. The dielectric constant of BIG is $\epsilon = 6.25$. Then, the off-diagonal term in the dielectric tensor of Eq. (1) is $\gamma = \theta_F \sqrt{\epsilon}\lambda / \pi = 0.069$ [19,20]. Diluted magnetic semiconductors with large magneto-optical effects ($\theta_F \sim 10^3$ rad/cm) have also been studied both theoretically and experimentally [34–39]. On the other hand, there is a magneto-optical material which shows larger Faraday rotations than in BIG. At $T = 20$ degrees Kelvin, the Faraday rotation angle of EuO is $\theta_F = 3.49 \times 10^3$ rad/cm at $\lambda = 1.5$ μm under a magnetic filed 0.9 Tesla. The dielectric constant of EuO is $\epsilon = 6.0$. In this case, the off-diagonal term in the dielectric tensor of Eq. (1) is $\gamma = 0.41$ [40–42]. In what follows, we use EuO as a guide to the magnitude of magneto-optical effects that can be realized in practice. In particular, we choose $\gamma = 0.41$ and we extrapolate this magneto-optical behavior to room temperature.

To realize a magnetic domain wall, strong magnetic fields in the opposite directions must be applied locally. Recently, a method of applying strong magnetic fields locally has been proposed theoretically in the field of spintronics [43]. Ferromagnetic materials such as Tb, Fe, and dysprosium (Dy) have strong magnetic fields and large magnetic gradients. In particular, when a magnetic slab [$|x| \leq d_x/2$, $|y| \leq d_y/2$ and $|z| \leq d_z/2$ ($d_x, d_y \gg d_z$)] of Dy is magnetized in the z direction, a strong magnetic field is generated near the edge of the magnetic slab [e.g., $|x| = d_x/2 + \Delta x$ (small $\Delta x > 0$), $z \sim 0$ or $|y| = d_y/2 + \Delta y$ (small $\Delta y > 0$), $z \sim 0$]: $|B_z| > 2.45$ Tesla with a large magnetic gradient $|\partial B_z / \partial x| \sim 10$ Tesla/μm at $T < 180$ K [43]. We assume that one magnetic slab, magnetized in the positive z direction, is placed above the nonreciprocal waveguide ($z > 0$) for $x < 0$, whereas the second magnetic slab, magnetized in the negative z direction, is placed below the nonreciprocal waveguide ($z < 0$) for $x > 0$. By applying these strong magnetic fields locally in opposite z directions, magnetic domain walls may be achieved in a photonic crystal membrane waveguide.

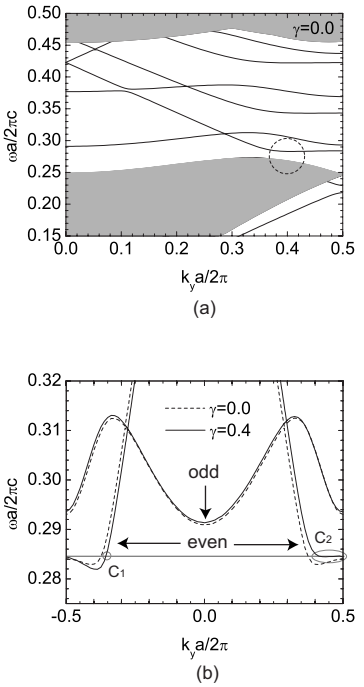

FIG. 4. (a) Guided modes of the waveguide calculated with 1815 plane waves by the PWE method at $\gamma = 0.0$. Solid lines are the guided modes, and shaded regions are the photonic band continua projected to k_y. A supercell is in the region of $|x|/a \leq 2.5\sqrt{3}$ and $|y|/a \leq 0.5$. (b) Guided modes of the waveguide in the frequency region of $0.275 \leq \omega a/2\pi c \leq 0.32$. Dotted and solid lines indicate the guided modes at $\gamma = 0.0$ (reciprocal) and $\gamma = 0.4$ (nonreciprocal), respectively. As described by arrows, there are even and odd modes. In the even and odd modes, distributions of guided modes are symmetric and antisymmetric, respectively, with respect to $x = 0$. These symmetries are valid for both $\gamma = 0.0$ and $\gamma = 0.4$. When focusing on $\omega a/2\pi c = 0.2845$ drawn by a gray line, there are two crossing points. C_1 and C_2 are the crossing points for $k_y < 0$ and $k_y > 0$, respectively.

B. Waveguide dispersion engineering

We consider TE guided modes of our idealized 2D nonreciprocal waveguide in Fig. 1. A supercell of the waveguide occupies the region of $|x|/a \leq 2.5\sqrt{3}$ and $|y|/a \leq 0.5$. Figure 4(a) shows the conventional guided modes of the waveguide calculated with 1815 plane waves by the PWE method at $\gamma = 0.0$. Solid lines are the guided modes, and shaded regions are the photonic band structures projected to k_y. The 2D triangular-lattice PC has a large PBG in the frequency of $0.2722 \leq \omega a/2\pi c \leq 0.4544$. As shown in this figure, there appear many guided modes in this PBG. Conventionally, guided modes change monotonically as $|k_y|$ approaches π/a. However, in the frequency region of $0.282 \leq \omega a/2\pi c$

$\leqslant 0.288$, the lowest dispersion branch has a local minimum near $|k_y| = 0.8\pi/a$. As the width, w, of the waveguide increases, frequencies of guided modes become lower. Eventually, the lowest guided mode interacts with lower shaded photonic bands, as indicated by a dotted circle in Fig. 4(a). As a result of this interaction, a guided mode with a local minimum is obtained. Robustness of this local minimum with respect to disorder is demonstrated at the end of this section.

The waveguide dispersion curve depicted in Fig. 4(b), exhibits significant nonreciprocity for nonzero γ. In the frequency region of $0.275 \leqslant \omega a/2\pi c \leqslant 0.32$, dotted and solid lines in Fig. 4(b) indicate the guided modes at $\gamma = 0.0$ (reciprocal) and $\gamma = 0.4$ (nonreciprocal), respectively. Arrows indicate even and odd parity optical modes. In the even and odd guided modes, field distributions are symmetric and antisymmetric, respectively, with respect to $x = 0$. These symmetries remain in effect for both $\gamma = 0.0$ and $\gamma = 0.4$. At $\gamma = 0.0$, ω is symmetric with respect to k_y, but for $\gamma = 0.4$, it is not. Even in the nonreciprocal case, ω is the same at $k_y = \pm \pi/a$, since magneto-optical effects preserve periodicity along the guiding direction (corresponding to a periodicity of $2\pi/a$ in k_y). In the frequency region of $0.282 \leqslant \omega a/2\pi c \leqslant 0.288$, frequencies for $k_y < 0$ and $k_y > 0$ become lower and higher, respectively. When focusing on $\omega a/2\pi c = 0.2845$ (highlighted by gray circles), there are two crossing points, C_1 and C_2, for $k_y < 0$ and $k_y > 0$, respectively. Forward and backward propagating light are identified by positive and negative group velocities, respectively. At C_1 the group velocity is positive, whereas at C_2 the group velocity is negative and close to zero. This means that forward light propagates rapidly in the positive y direction whereas backward light stops.

C. Nonreciprocal transmission and reflection characteristics

To illustrate the one-way waveguide effect, we investigate light propagation in the nonreciprocal PC waveguide without absorption by the FDTD method. We take $\Delta x/a = \Delta y/a = 0.01$ and $c\Delta t/a = 0.005$ as our discretizations of time and space. Unlike in conventional PC waveguides, very fine discretizations are required in nonreciprocal PC waveguides to describe light propagation with nearly zero group velocity. Figures 5(a) and 5(b) show distributions of magnetic fields in the z direction after 18 000 time steps in forward and backward light, respectively, at $\omega a/2\pi c = 0.2845$. Dotted lines indicate the position of magnetic domain walls. The nonreciprocal waveguides occupy the regions $|x|/a \leqslant \sqrt{3}/2$ and $|y|/a \leqslant 7.5$. In Figs. 5(a) and 5(b), point sources (indicated by solid circles) are placed at $(x/a, y/a) = (0.0, -8.0)$ and (0.0,8.0), respectively. In Fig. 5(a) forward light is transmitted through the waveguide. In Fig. 5(b) backward light stops because of nearly zero group velocity. In practice, however, there is a slow leakage of backward light in the absence of absorption because the group velocity is not exactly zero.

We investigate transmittance and reflectance of forward and backward light through the nonreciprocal waveguide segment using the WF method [31,32]. The region bounded by $|x|/a \leqslant 2.5\sqrt{3}$ and $|y|/a \leqslant 0.5$ in Fig. 1 is chosen as a supercell to construct maximally localized WF basis functions.

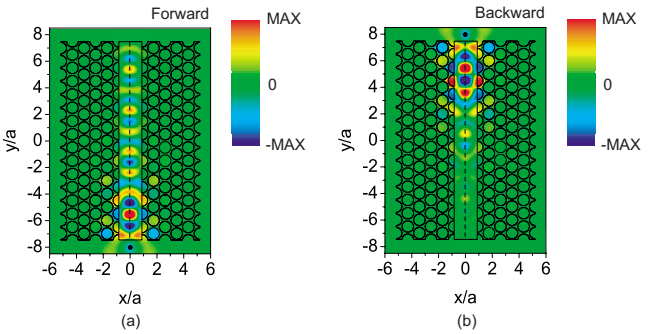

FIG. 5. (Color online) Distributions of magnetic fields in the z direction at 18 000 time steps in forward and backward light with $\omega a/2\pi c = 0.2845$, respectively, by the FDTD method. Dotted lines are magnetic domain walls. In (a) and (b), point sources drawn by black circles of forward and backward light are at $(x/a, y/a) = (0.0, -8.0)$ and (0.0,8.0), respectively.

In Eq. (16), we take $\epsilon = 6.0$ and $\gamma = 0.0$ in light shaded regions of waveguides of Fig. 1 to define $\epsilon_p(\mathbf{r})$. We construct maximally localized WF's that precisely reproduce the guided modes depicted by dotted lines in Fig. 4(b). This requires 12 WF's in total, constructed from 10 bands, for $\omega a/2\pi c \leqslant 0.275$, and 2 bands for $\omega a/2\pi c \geqslant 0.275$.

In Fig. 6, we show the guided modes of reciprocal ($\epsilon = 6.15$, $\gamma = 0$) and nonreciprocal ($\epsilon = 6.0$, $\gamma = 0.4$) waveguides without absorption. Dotted and solid lines indicate the guided modes in the reciprocal and nonreciprocal waveguides, respectively, calculated with 1815 plane waves by the PWE method. The open and solid circles indicate the guided modes in reciprocal and nonreciprocal waveguides, respectively, calculated by the WF method. Clearly, the results of the PWE and WF methods coincide almost perfectly. In the region enclosed by a gray circle, guided modes of forward light coincide in the reciprocal and nonreciprocal waveguides. Single-mode guiding in the reciprocal

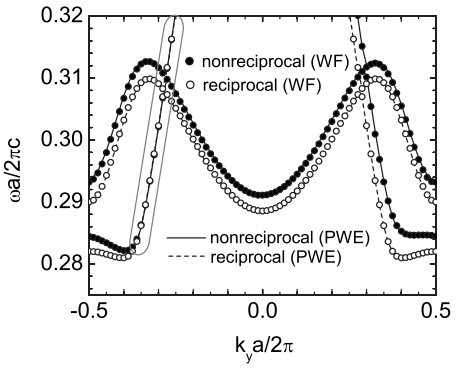

FIG. 6. Guided modes of reciprocal (dashed lines) and nonreciprocal (solid lines) waveguides without absorption, calculated with 1815 plane waves by the PWE method. The guided mode in the nonreciprocal waveguide is the same as that drawn by a solid line in Fig. 4(b). On the other hand, white and black circles indicate the guided modes in reciprocal and nonreciprocal waveguides, respectively, calculated by the Wannier function (WF) method. In the region highlighted on the left by a gray circle, guided modes of forward light coincide in the reciprocal and nonreciprocal waveguides.

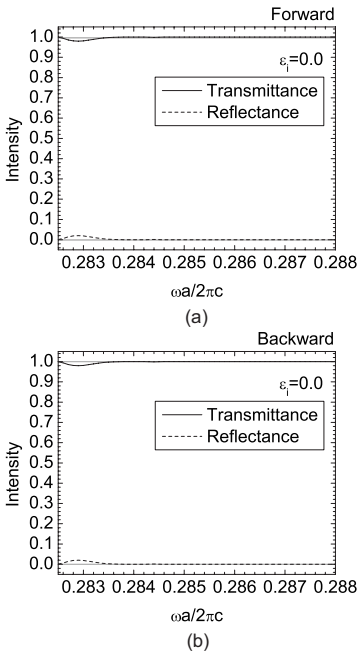

FIG. 7. Transmittance and reflectance in the coupling of reciprocal and nonreciprocal waveguides without absorption in Fig. 3. In the nonreciprocal waveguide, ϵ_i=0.0. (a) and (b) indicate the transmittance and reflectance in forward and backward light, respectively. Solid and dashed lines indicate the transmittance and reflectance, respectively.

waveguides occurs in the frequency region of $0.2819 \leqslant \omega a/2\pi c \leqslant 0.2883$. This usable frequency range corresponds to a bandwidth of about 34 nm centered at 1.5 micron wavelength.

Figure 7 depicts the transmittance and reflectance characteristics of a 20 unit cell long on-chip isolator (Fig. 3) in the absence of absorption. In the nonreciprocal waveguide, ϵ_i =0.0 (Sec. II B). Figures 7(a) and 7(b) indicate the transmittance (solid curves) and reflectance (dotted curves) in forward and backward light, respectively, calculated by the WF method. In both forward and backward light, the steady states of transmittance and reflectance are the same, in spite of nonreciprocity of the waveguide. We denote transmission and reflection coefficients of forward light by t and r, respectively, Transmittance and reflectance of forward light are denoted by $T^{(f)}=|t|^2$ and $R^{(f)}=|r|^2$, respectively. Transmission and reflection coefficients of backward light can be represented as $te^{i\alpha}$ and $re^{i\beta}$, respectively. Transmittance and reflectance of backward light are $T^{(b)}=|te^{i\alpha}|^2=|t|^2$ and $R^{(b)}=|re^{i\beta}|^2=|r|^2$, respectively. Although $T^{(f)}=T^{(b)}$ and $R^{(f)}=R^{(b)}$, field distributions and temporal behaviors of forward and backward light are different in the nonreciprocal waveguide. Nevertheless, in Fig. 5(b) backward light propagates with the same total transmittance as forward light after sufficient time has elapsed. Transmittance is mostly 1 and reflectance is mostly 0 for $\omega a/2\pi c \geqslant 0.2833$, where guided modes of reciprocal and nonreciprocal waveguides coincide.

Next, we consider the coupling of reciprocal and nonreciprocal waveguides (as depicted in Fig. 3) with absorption described by ϵ_i=0.015 (Sec. II B). Figures 8(a) and 8(b) indicate the transmittance and reflectance in forward and backward light, respectively, calculated by the WF method. Transmittance is lower than unity because of absorption, whereas reflectance is mostly zero. Due to nonreciprocity, transmittance of backward light is lower than that of forward light. Especially, at $\omega a/2\pi c$=0.2843, transmittance of backward light approaches zero because of near vanishing group velocity. In Fig. 5, we choose $\omega a/2\pi c$=0.2845, the point of minimum group velocity. This minimum point is now shifted to slightly lower frequency due to the effects of ϵ_i. Figure 8(c) shows the ratio of transmittance of backward light to that of forward light. $T^{(b)}/T^{(f)}$ also represents the total transmittance of backward light when transmittance of forward light is amplified to unity by current injection.

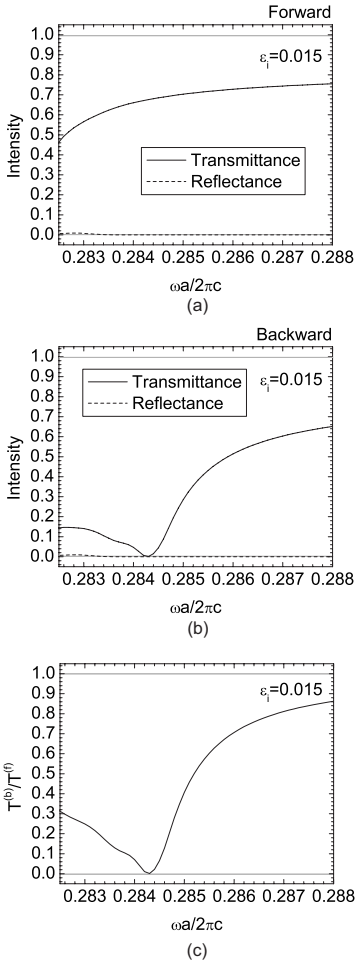

FIG. 8. Transmittance and reflectance in the one-way waveguide isolator of Fig. 3, including absorption. In the nonreciprocal waveguide, the imaginary part of the dielectric constant is chosen to be ϵ_i=0.015. (a) and (b) indicate the transmittance and reflectance in forward and backward light, respectively. Solid and dotted lines indicate the transmittance and reflectance, respectively. (c) shows the ratio of transmittance of backward light to that of forward light. This is equivalent to the backward transmission when the forward light transmission is renormalized to unity by current injection induced gain. $T^{(f)}$ and $T^{(b)}$ indicate the transmittance of forward and backward light, respectively.

In Figs. 9(a) and 9(b), we show distributions of absolute values of electric fields in forward and backward light, respectively, at $\omega a/2\pi c$=0.2843. In Fig. 9(a), transmittance of

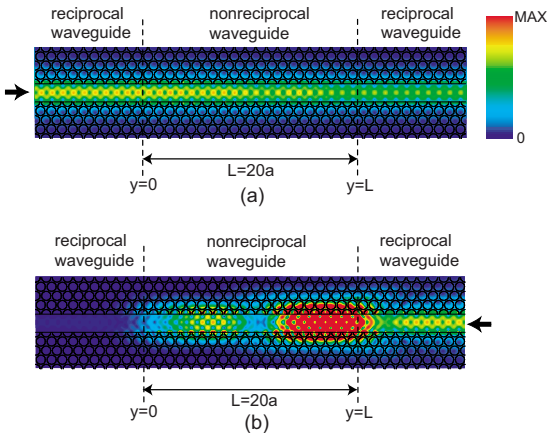

FIG. 9. (Color online) Distributions of absolute values of electric fields in (a) forward and (b) backward light at $\omega a/2\pi c = 0.2843$.

forward light is attenuated slowly. In Fig. 9(b), on the other hand, backward light decays rapidly. This occurs since $|\delta k^{(b)}|$ is much larger than $|\delta k^{(f)}|$ (Sec. II B) in the presence of magneto-optical activity. A loss of forward light can be compensated by current injection in the left reciprocal waveguide.

Figure 10 shows the ratio of transmittance of backward light to that of forward light as a function of ϵ_i for a fixed length $L=20a$ of nonreciprocal waveguide. Solid and dashed lines indicate $\omega a/2\pi c=0.2843$ and $\omega a/2\pi c=0.288$, respectively. $T^{(b)}/T^{(f)}$ at $\omega a/2\pi c=0.2843$ decreases rapidly with increasing ϵ_i. On the other hand, $T^{(b)}/T^{(f)}$ at $\omega a/2\pi c = 0.288$ decreases much more slowly. This is because in backward light the group velocity of $\omega a/2\pi c=0.2843$ is much smaller than that of $\omega a/2\pi c=0.288$.

Figure 11 shows the ratio of transmittance of backward light to that of forward light as a function of $L/a=20$, 50, 100, 200, and 900. $T^{(b)}/T^{(f)}$ decreases with increasing L. As shown in this figure, we must take a very long nonreciprocal waveguide of $L/a=900$ to efficiently decrease the transmittance in the entire frequency region. As shown in Fig. 8(c), at $\omega a/2\pi c=0.288$ absorption in backward light is not very large, because of a nonzero group velocity. When setting up $\omega a/2\pi c=a/\lambda=0.2843$ as $\lambda=1.5$ μm, $a=426.45$ nm. The usable bandwidth $0.2819\leqslant\omega a/2\pi c\leqslant 0.2883$ corresponds to

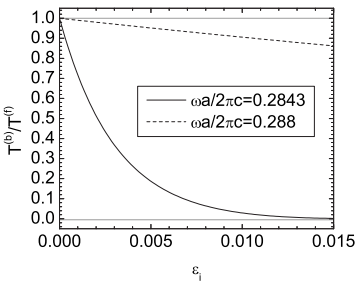

FIG. 10. Ratio of transmittance of backward light to that of forward light as a function of the imaginary part of the dielectric constant ϵ_i, in the nonreciprocal waveguide segment. Solid and dotted lines indicate $\omega a/2\pi c=0.2843$ and $\omega a/2\pi c=0.288$, respectively.

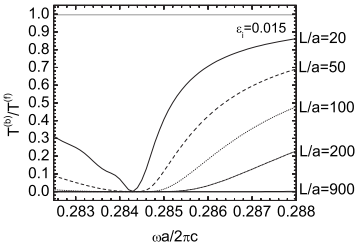

FIG. 11. Ratio of transmittance of backward light to that of forward light as a function of the length of the nonreciprocal waveguide segment. Depicted are $L/a=20$, 50, 100, 200, and 900.

1.48 μm$\leqslant\lambda\leqslant 1.51$ μm. Then, $L/a=20$ and 900 correspond to $L=8.5$ μm and 383.8 μm, respectively. In other words, this nonreciprocal waveguide with a zero group velocity enables a compact on-chip PBG isolator, whose usable bandwidth increases with the length of the nonreciprocal segment.

D. Tapered nonreciprocal waveguide

A key issue in the functionality of the on-chip isolator is the bandwidth over which high contrast one-way waveguiding can be sustained. In the designs described above, the group velocity for backward light becomes nearly zero over a small band near a specific frequency. This frequency point, in turn, depends on the structural properties of the waveguide such as its width and dielectric constant. In this section we consider a simple approach to varying the frequency point for vanishing group velocity along the length of nonreciprocal waveguide by introducing a gradual variation of waveguide structure along the length of the waveguide. In this way, a larger bandwidth for efficient absorption of backward light may be realized inside a nonreciprocal waveguide segment of length $L/a=100$ ($L=42.6$ μm).

For zero backward group velocity to span the entire frequency range $0.2825\leqslant\omega a/2\pi c\leqslant 0.288$, we consider the gradual change of dielectric constant $\epsilon(y)=5.8+0.2(y-L/2)^2/(L/2)^2$ [$\epsilon(0)=6.0$, $\epsilon(50a)=5.8$ and $\epsilon(100a)=6.0$] in the nonreciprocal waveguide ($\gamma=0.4$). When the dielectric constant of the nonreciprocal waveguide becomes lower, the frequency point of nearly zero group velocity becomes higher. At $\epsilon=5.8$ and 6.0 the frequency of nearly zero group velocity is $\omega a/2\pi c\sim 0.2875$ and 0.2845, respectively. The gradual change of ϵ forces backward light to encounter a zero group velocity point throughout the frequency range $0.2845\leqslant\omega a/2\pi c\leqslant 0.2875$. On the other hand, $T^{(b)}/T^{(f)}\sim 0$ for a nonreciprocal tapered waveguide of length $L/a=100$ in the frequency region of $0.2825\leqslant\omega a/2\pi c\leqslant 0.2848$ when $\epsilon=6.0$, as shown in Fig. 11. For the practical dielectric modulation specified above, reflectance of forward light becomes large in the frequency region of $0.2825\leqslant\omega a/2\pi c\leqslant 0.2845$, whereas $T^{(b)}/T^{(f)}$ is mostly zero in the frequency region of $0.2845\leqslant\omega a/2\pi c\leqslant 0.2874$. Therefore, either an antireflection architecture must be introduced at the entrance port of forward light or an improved waveguide design must be found in order to achieve $T^{(b)}/T^{(f)}\sim 0$ throughout the entire frequency range $0.2825\leqslant\omega a/2\pi c\leqslant 0.288$.

E. Isolator without magnetic domain wall

In Fig. 1 we used a magnetic domain wall to break space-inversion symmetry. In practice it is simpler to apply strong

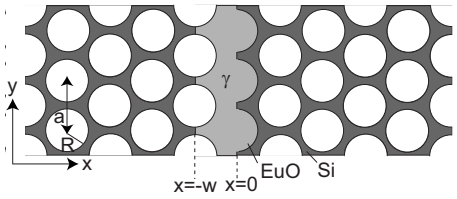

FIG. 12. Structure of an asymmetric nonreciprocal waveguide without any magnetic domain wall in a 2D triangular-lattice PC composed of air holes in a Si substrate. This structure has broken space-inversion symmetry. Dark and light shaded regions indicate Si and EuO, respectively. $w/a=\sqrt{3}/2$. 2D triangular-lattice PC's in backgrounds are the same as those in Fig. 1. In the light shaded region, $\gamma(\mathbf{r})=\gamma$.

magnetic field in just one direction. In Fig. 12, we introduce an asymmetric nonreciprocal waveguide, without a magnetic domain wall, in a 2D triangular-lattice PC composed of air holes in a Si substrate. This structure has no space-inversion symmetry. Dark and light shaded regions indicate Si and EuO, respectively. $w/a=\sqrt{3}/2$. The 2D triangular-lattice PC in background is the same as that in Fig 1. In the light shaded region, $\gamma(\mathbf{r})=\gamma$. This architecture enables a nonreciprocal waveguide without a magnetic domain wall.

Figure 13 shows the guided modes of the waveguide calculated with 1815 plane waves by the PWE method. Our supercell is chosen to occupy the region of $|x|/a \leqslant 2.5\sqrt{3}$ and $|y|/a \leqslant 0.5$. Dotted and solid lines indicate the guided modes at $\gamma=0.0$ (reciprocal) and $\gamma=0.4$ (nonreciprocal). At $\gamma=0.0$, ω is symmetric with respect to k_y. At $\gamma=0.4$, ω is not symmetric with respect to k_y. Near $\omega a/2\pi c=0.3060$ (highlighted by a gray circle), the group velocity is positive for $k_y<0$ (region C_1), whereas for $k_y>0$ (region C_2) the group velocity is mostly zero.

We consider the coupling of reciprocal and nonreciprocal waveguides as in Fig. 3. In the reciprocal waveguide, we take $\epsilon_D=6.15$ and $\gamma=0.0$. Single-mode waveguiding in the reciprocal waveguides occurs in the range $0.3037 \leqslant \omega a/2\pi c \leqslant 0.3514$. This defines the operating bandwidth of the isolator. In the nonreciprocal waveguide, we choose $\epsilon_i=0.015$ (Sec. II B). In Fig. 14, we show the transmittance

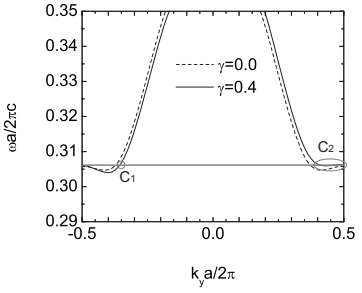

FIG. 13. Guided modes of the waveguide in Fig. 12 calculated with 1815 plane waves by the PWE method. A supercell is in the region of $|x|/a \leqslant 2.5\sqrt{3}$ and $|y|/a \leqslant 0.5$. Dotted and solid lines indicate the guided modes at $\gamma=0.0$ (reciprocal) and $\gamma=0.4$ (nonreciprocal), respectively. When focusing on $\omega a/2\pi c=0.3060$ drawn by a gray line, there are two crossing points highlighted by gray circles. C_1 and C_2 are the crossing points for $k_y<0$ and $k_y>0$, respectively.

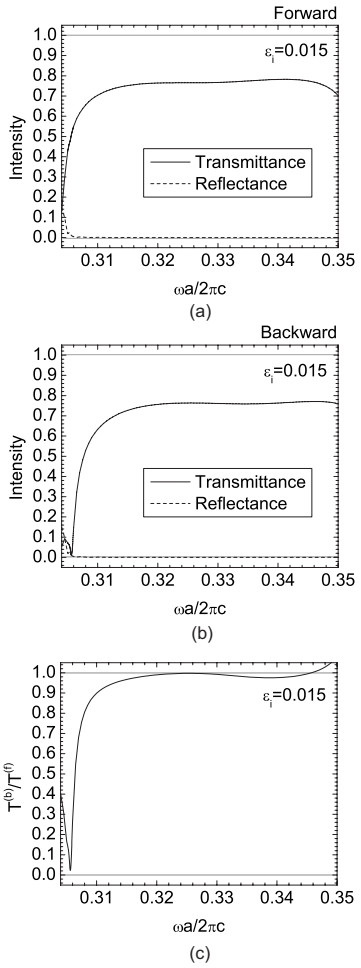

FIG. 14. Transmittance and reflectance in the asymmetric one-way waveguide isolator of Fig. 12 with absorption. In the nonreciprocal waveguide, $\epsilon_i=0.015$. (a) and (b) indicate the transmittance and reflectance in forward and backward light, respectively. Solid and dotted lines indicate the transmittance and reflectance, respectively. (c) shows the ratio of transmittance of backward light to that of forward light. This is equivalent to the backward transmission when the forward light transmission is renormalized to unity by current injection induced gain. $T^{(f)}$ and $T^{(b)}$ are the transmittance of forward and backward light, respectively.

and reflectance characteristics of this isolator calculated by the WF method. Nonreciprocity between forward and backward light is clearly evident near $\omega a/2\pi c \geqslant 0.3056$. Transmittance is lower than 1 because of absorption. Reflectance is negligible for $\omega a/2\pi c \geqslant 0.305$, but is nonzero for $\omega a/2\pi c < 0.305$ due to the mismatch between the reciprocal and nonreciprocal waveguides. At $\omega a/2\pi c=0.3056$, transmittance of backward light is extremely low because of its zero group velocity. In Fig. 13, we focused on $\omega a/2\pi c=0.3060$. However, the frequency of the zero group velocity point is now slightly different because of ϵ_i. Figure 14(c) shows the ratio of transmittance of backward light to that of forward light. $T^{(f)}$ and $T^{(b)}$ indicate the transmittance of forward and backward light, respectively. Unlike in Fig. 8(c), $T^{(b)}/T^{(f)}$ exceeds 1 for $\omega a/2\pi c > 0.346$. This is because the group velocity of backward light is larger than that of forward light for $\omega a/2\pi c > 0.346$. In the waveguide isolator

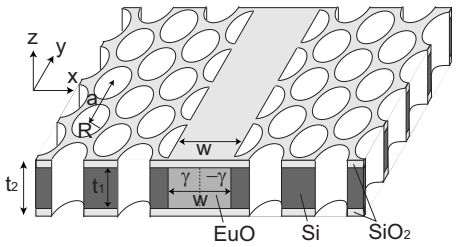

FIG. 15. Structure of a 2D triangular-lattice membrane PC with a nonreciprocal waveguide. The idealized 2D structure in Fig. 1 is now sandwiched above and below by thin SiO_2 glass. The background is the air. The thickness of the 2D triangular-lattice PC composed of Si is $t_1/a=0.8$, and the thickness of the overall 2D triangular-lattice membrane PC is $t_2/a=1.2$. The dielectric constant of SiO_2 is $\epsilon=2.25$. The radius of air holes is $R/a=0.43$. The waveguide has a magnetic domain wall. At $x=0$ and $|z|\leq t_1/2$, there is a magnetic domain wall drawn by a dotted line. For $-\sqrt{3}/2<x/a<0$ and $|z|\leq t_1/2$, and $0<x/a<\sqrt{3}/2$ and $|z|\leq t_1/2$, $\gamma(\mathbf{r})=\gamma$ and $\gamma(\mathbf{r})=-\gamma$, respectively, in Eq. (1). Otherwise, $\gamma(\mathbf{r})=0$. In the 2D membrane PC, white regions indicate the air holes. This structure is symmetric about the plane $z=0$.

with a magnetic domain wall, the bandwidth (see Fig. 8) is considered as the frequency range with $T^{(b)}/T^{(f)}<0.86$. In the waveguide isolator considered in this section, on the other hand, the bandwidth with $T^{(b)}/T^{(f)}<0.86$ is the frequency range $0.305<\omega a/2\pi c<0.309$. The bandwidth without a magnetic domain wall is slightly narrower than that with the magnetic domain wall described in Fig. 8.

F. One-way waveguide in PC membrane

In this section, we demonstrate optical waveguide isolators in the realistic three-dimensional (3D) context of a 2D membrane PC. Figure 15 shows the structure of a 2D triangular-lattice membrane PC with a nonreciprocal waveguide. A structure in Fig. 1 is sandwiched with SiO_2 glass and the entire membrane is surrounded by air. The thickness of the 2D triangular-lattice PC composed of Si is $t_1/a=0.8$ and a thickness of an overall membrane is $t_2/a=1.2$. The dielectric constant of SiO_2 is $\epsilon=2.25$, the radius of air holes is $R/a=0.43$, and the waveguide has a magnetic domain wall at $x=0$ for $|z|\leq t_1/2$ (dotted line in Fig. 15). For $-\sqrt{3}/2<x/a<0$, and $0<x/a<\sqrt{3}/2$, $\gamma(\mathbf{r})=\gamma$ and $\gamma(\mathbf{r})=-\gamma$, respectively, for $|z|\leq t_1/2$. Otherwise, $\gamma(\mathbf{r})=0$. In the 2D membrane PC, white regions indicate the air holes. This structure is symmetric about the plane $z=0$.

Figure 16 shows the guided even modes (in which the z component of magnetic fields is symmetric about the plane $z=0$), calculated with 7175 plane waves by the PWE method. The even modes are similar to 2D TE modes. Our supercell for this calculation occupies the region of $|x|/a\leq 2\sqrt{3}$, $|y|/a\leq 0.5$ and $|z/a|\leq 2$. Dotted and solid lines indicate the guided modes at $\gamma=0.0$ and $\gamma=0.4$, respectively. A dark shaded region indicates the light cone in which light leaks vertically into the surrounding air. At $\gamma=0.0$, we obtain the guided modes with dispersion minima near $|k_y|=0.8\pi/a$. This zero group velocity condition is similar to that described in Fig. 4. At $\gamma=0.4$, ω is not symmetric with respect to k_y. When focusing on $\omega a/2\pi c=0.3220$ (highlighted by gray circles), there are two crossing points, C_1 and C_2 for $k_y<0$ and $k_y>0$, respectively. At C_1 the group velocity is positive, whereas at C_2 the group velocity is negative and nearly zero. This suggests that compact on-chip PBG isolators can be obtained for realistic 2D membrane PC's in three dimensions.

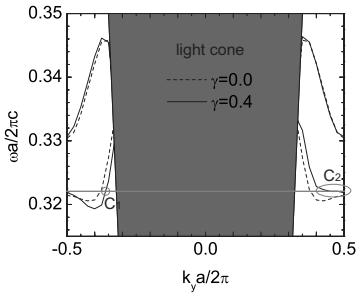

FIG. 16. Guided even modes, in which the z component of magnetic fields is symmetric about the plane $z=0$, calculated with 7175 plane waves by the PWE method. Dotted and solid lines indicate the guided modes at $\gamma=0.0$ and $\gamma=0.4$, respectively. A dark shaded region indicates the light cone in which light leaks vertically out of the membrane into air regions. At $\gamma=0.4$, ω is not symmetric with respect to k_y. When focusing on a gray line, there are two crossing points highlighted by gray circles. C_1 and C_2 are the crossing points for $k_y<0$ and $k_y>0$, respectively.

G. Robustness to structural variations

A key feature in the realization of nonreciprocal behavior in our model is the existence of a local minimum (apart from $k_y=0$ and $k_y=\pm\pi/a$) in the single-mode region of the waveguide dispersion. In this section, we examine the robustness of this local minimum to small variations in waveguide parameters. This, in turn, determines the robustness of our isolator functionalitiy to random disorder. We consider the robustness (at $\gamma=0$) of the waveguide dispersion minimum to variations in the radii of air holes and width of waveguide (see Fig. 1). In Fig. 17, we show the robustness of the local minimum with respect to radii of air holes for EuO waveguides with $w/a=\sqrt{3}$. Figures 17(a)–17(f) show the guided modes at $R/a=0.4$, 0.41, 0.42, 0.43, 0.44, and 0.445, respectively. Shaded regions indicate the photonic bands projected to k_y and dotted lines indicate the frequencies at $|k_y|=\pi/a$. With increasing R/a, frequencies of the guided modes become higher but closer to the (more rapidly rising) photonic bands in the shaded regions. At $R/a=0.4$ the curve is mostly flat, at $R/a=0.43$ the dispersion minimum is deeper, and at $R/a=0.445$ the curve is again mostly flat. The required dispersion minimum effect remains valid for $0.42\leq R/a\leq 0.44$.

In Fig. 18, we show the robustness of the dispersion minimum to waveguide width variations at $\gamma=0.0$ for the 2D triangular-lattice PC composed of air holes with $R/a=0.43$. We consider EuO waveguides of various widths, w. Figures 18(a)–18(f) show the guided modes at $w/a=0.7\sqrt{3}$, $0.8\sqrt{3}$, $0.9\sqrt{3}$, $\sqrt{3}$, $1.05\sqrt{3}$, and $1.1\sqrt{3}$, respectively. Shaded regions indicate the lower photonic band continuum projected to k_y,

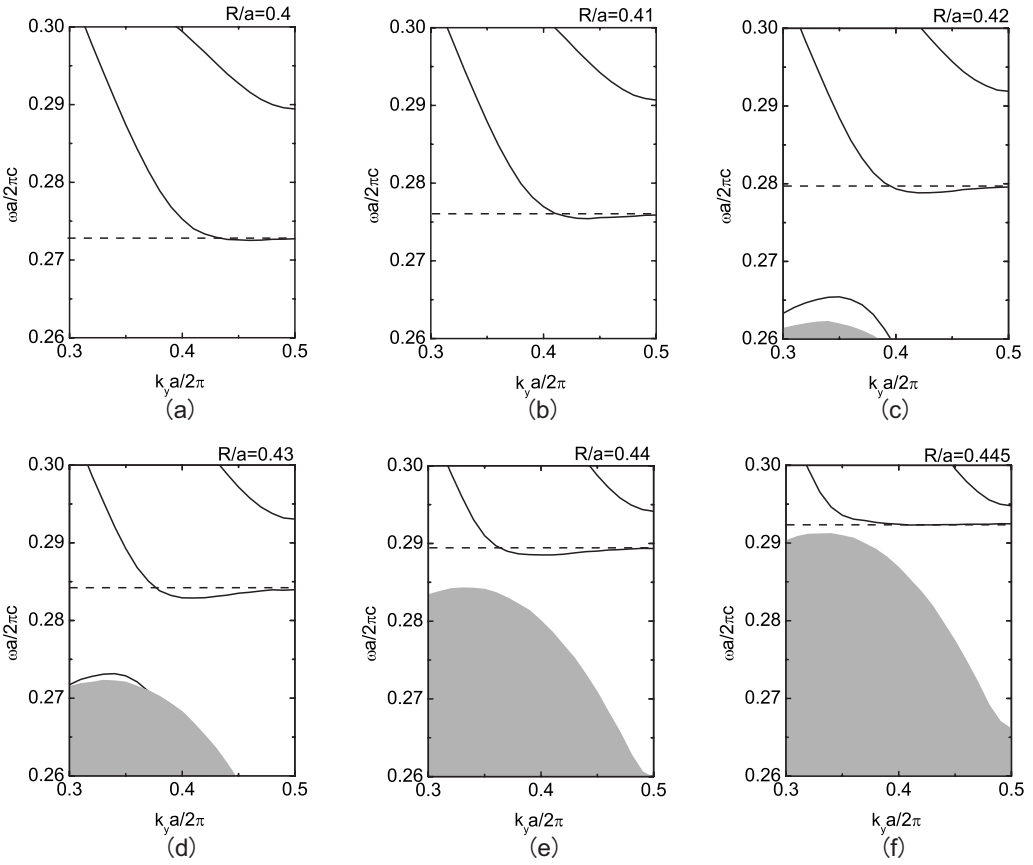

FIG. 17. Robustness at $\gamma=0.0$ of the waveguide dispersion minimum with respect to radii of air holes for waveguides for $w/a=\sqrt{3}$. (a)–(f) show the guided modes at $R/a=0.4$, 0.41, 0.42, 0.43, 0.44, and 0.445, respectively. Shaded regions indicate the photonic band continua projected to k_y, and dotted lines indicate the frequencies at $|k_y|=\pi/a$.

and dotted lines indicate the frequency at $|k_y|=\pi/a$. With increasing w/a, frequencies of the guided modes become lower and two guided modes become closer. At $w/a=0.7\sqrt{3}$ the curve is mostly flat, whereas at $w/a=1.1\sqrt{3}$ the two guided modes coalesce and single-mode waveguiding is lost. The required dispersion characteristics remain valid for $0.9\sqrt{3}\leqslant w/a\leqslant 1.05\sqrt{3}$.

In summary, the waveguide characteristics required for optical isolator functionality are robust to variations in hole radius in the range $0.42\leqslant R/a\leqslant 0.44$ and variations in the waveguide width over the range $0.9\sqrt{3}\leqslant w/a\leqslant 1.05\sqrt{3}$.

V. CONCLUSIONS

We have demonstrated the integration of one-way optical waveguide isolators in two-dimensional photonic crystal circuits. This nonreciprocal waveguide consists of a magneto-optical material in which spatial inversion symmetry is broken. At a specific frequency, backward light in this waveguide exhibits zero group velocity, whereas forward light propagates rapidly.

To illustrate the characteristics of this isolator, we have simulated light propagation of forward and backward light using both the FDTD and WF methods. In order to eliminate slow leakage of backward light through our nonreciprocal waveguide, we introduced absorption. To compensate for the small absorption of forward light, amplification by current injection was required.

In our optical waveguide isolator, the useful bandwidth (where the ratio of backward to forward light transmission $T^{(b)}/T^{(f)}$ is nearly zero) increases with the length of the nonreciprocal segment. This bandwidth ranges from a few nanometers when the nonreciprocal region is less than 10 micron up to 12 nm when the nonreciprocal region is more than 40 microns. Near the zero group velocity point for backward light, $T^{(b)}/T^{(f)}$ decreases rapidly with increasing isolator length. To widen the bandwidth in short nonreciprocal waveguides, we considered a gradual change of dielectric constants in the nonreciprocal waveguides in order to adiabatically vary the zero group velocity point over a range of frequencies along the length of the isolator. However, this produced unwanted reflections. Therefore, either an antireflection architecture must be introduced at the entrance port of forward light or an improved waveguide design must be found in order to achieve $T^{(b)}/T^{(f)}\sim 0$ throughout the entire frequency range. It is possible that with further design optimization, a larger bandwidth can be accomodated within a more compact device architecture. We have shown the robustness of our waveguide dispersion minimum to structural variations of the waveguide architecture. From these results,

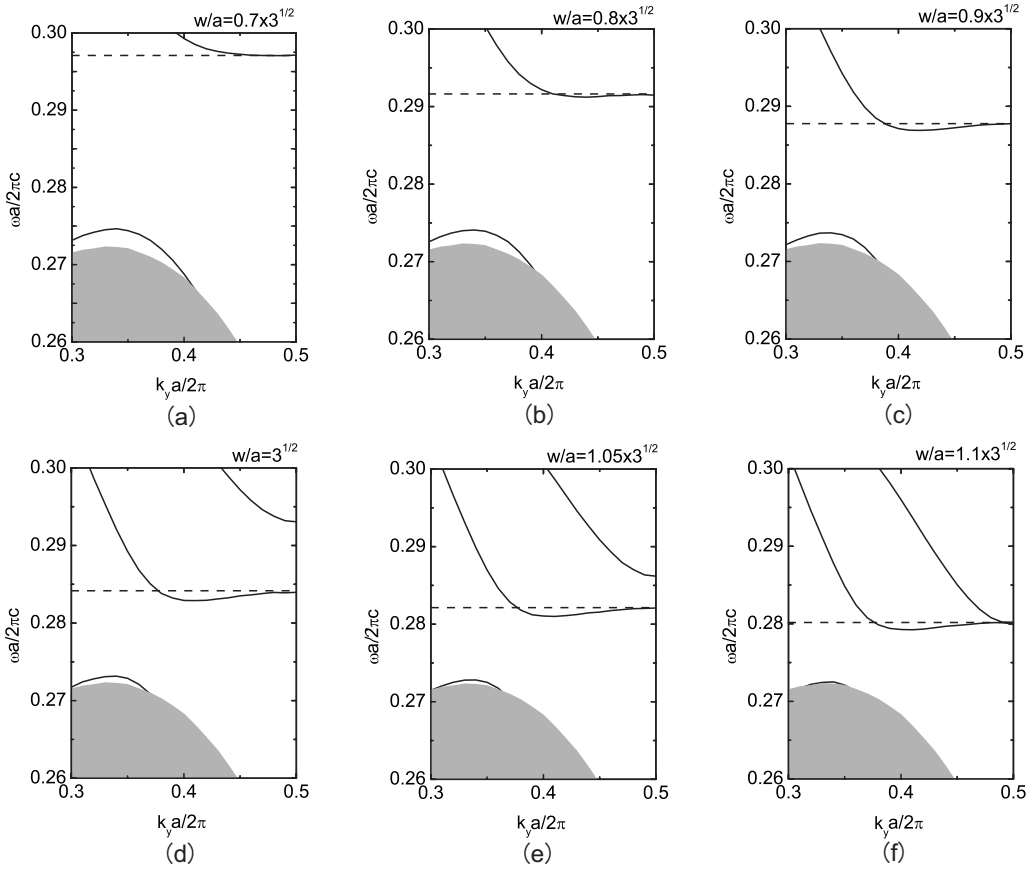

FIG. 18. Robustness at $\gamma=0.0$ of the waveguide dispersion minimum with respect to widths of waveguides for 2D triangular-lattice PC's composed of air holes with $R/a=0.43$. (a)–(f) show the guided modes at $w/a=0.7\sqrt{3}$, $0.8\sqrt{3}$, $0.9\sqrt{3}$, $\sqrt{3}$, $1.05\sqrt{3}$, and $1.1\sqrt{3}$, respectively. Shaded regions indicate the photonic band continua projected to k_y, and dotted lines indicate the frequencies at $|k_y|=\pi/a$.

we expect an equivalent robustness to random disorder.

For computational simplicity, we have considered TE modes in 2D photonic crystals in which electric fields are in the 2D xy plane. However, the same principles of broken time-reversal and space-inversion symmetries should apply to other geometries. For instance, in 2D-3D PBG heterostructures [44,45], waveguide modes have a predominantly TM character, with electric fields in the z direction. To realize optical waveguide isolators for TM modes, magneto-optical materials should be magnetized in the 2D xy plane, and space-inversion symmetry should be broken in the z direction. Such architectures must be incorporated into 2D-3D PBG heterostructures in which TM guided modes are engineered with the required dispersion minimum. This would then fulfill one of the key requirements for large-scale integrated optics in 3D photonic band gap microchips.

ACKNOWLEDGMENTS

This work was supported in part by the Natural Sciences and Engineering Research Council of Canada, the Canadian Institute for Advanced Research and a grant from the Premier of Ontario.

APPENDIX: NONRECIPROCITY USING BOTH BROKEN TIME-REVERSAL AND SPACE-INVERSION SYMMETRIES

Time-reversal symmetry

Time-reversal symmetry is present provided that $\gamma(\mathbf{r})=0$ in Eq. (1). Substituting Eqs. (1) and (4) into Eq. (3), we obtain

$$(\nabla + i\mathbf{k}) \times [\epsilon(\mathbf{r})^{-1}(\nabla + i\mathbf{k}) \times \mathbf{h}_{n\mathbf{k}}(\mathbf{r})] = \frac{\omega_{n\mathbf{k}}^2}{c^2}\mathbf{h}_{n\mathbf{k}}(\mathbf{r}). \tag{A1}$$

Taking $\mathbf{k} \rightarrow -\mathbf{k}$ and the complex conjugate in Eq. (A1),

$$(\nabla + i\mathbf{k}) \times [\epsilon(\mathbf{r})^{-1}(\nabla + i\mathbf{k}) \times \mathbf{h}_{n-\mathbf{k}}^*(\mathbf{r})] = \frac{\omega_{n-\mathbf{k}}^2}{c^2}\mathbf{h}_{n-\mathbf{k}}^*(\mathbf{r}). \tag{A2}$$

In Eqs. (A1) and (A2), operators are the same. Therefore, we can consider $\mathbf{h}_{n\mathbf{k}}(\mathbf{r})=\mathbf{h}_{n-\mathbf{k}}^*(\mathbf{r})$ and $\omega_{n\mathbf{k}}=\omega_{n-\mathbf{k}}$, regardless of $\epsilon(\mathbf{r})=\epsilon(-\mathbf{r})$ or $\epsilon(\mathbf{r}) \neq \epsilon(-\mathbf{r})$. In other words, in the presence of time-reversal symmetry frequencies are symmetric with respect to wave vectors (reciprocal), regardless of the exis-

tence or the breaking space-inversion symmetry.

Breaking of time-reversal symmetry

In order to break time-reversal symmetry, we allow $\gamma(\mathbf{r}) \neq 0$ in Eq. (1). Substituting Eqs. (1) and (4) into Eq. (3), we obtain

$$(\nabla + i\mathbf{k}) \times \{\boldsymbol{\epsilon}^{-1}(\mathbf{r}) \cdot [(\nabla + i\mathbf{k}) \times \mathbf{h}_{n\mathbf{k}}(\mathbf{r})]\} = \frac{\omega_{n\mathbf{k}}^2}{c^2}\mathbf{h}_{n\mathbf{k}}(\mathbf{r}), \tag{A3}$$

where

$$\boldsymbol{\epsilon}(\mathbf{r}) = \begin{bmatrix} \epsilon(\mathbf{r}) & -i\gamma(\mathbf{r}) & 0 \\ i\gamma(\mathbf{r}) & \epsilon(\mathbf{r}) & 0 \\ 0 & 0 & \epsilon(\mathbf{r}) \end{bmatrix}. \tag{A4}$$

Taking $\mathbf{k} \to -\mathbf{k}$ and $\mathbf{r} \to -\mathbf{r}$ in Eq. (A3),

$$(\nabla + i\mathbf{k}) \times \{\boldsymbol{\epsilon}^{-1}(-\mathbf{r}) \cdot [(\nabla + i\mathbf{k}) \times \mathbf{h}_{n-\mathbf{k}}(-\mathbf{r})]\} = \frac{\omega_{n-\mathbf{k}}^2}{c^2}\mathbf{h}_{n-\mathbf{k}}(-\mathbf{r}), \tag{A5}$$

where

$$\boldsymbol{\epsilon}(-\mathbf{r}) = \begin{bmatrix} \epsilon(-\mathbf{r}) & -i\gamma(-\mathbf{r}) & 0 \\ i\gamma(-\mathbf{r}) & \epsilon(-\mathbf{r}) & 0 \\ 0 & 0 & \epsilon(-\mathbf{r}) \end{bmatrix}. \tag{A6}$$

In an architecture with space-inversion symmetry $\epsilon(\mathbf{r}) = \epsilon(-\mathbf{r})$ and $\gamma(\mathbf{r}) = \gamma(-\mathbf{r})$, the operators are the same in Eqs. (A3) and (A5). Therefore, we can consider $\mathbf{h}_{n\mathbf{k}}(\mathbf{r}) = \mathbf{h}_{n-\mathbf{k}}(-\mathbf{r})$ and $\omega_{n\mathbf{k}} = \omega_{n-\mathbf{k}}$. In other words, even with broken time-reversal symmetry, frequencies are symmetric with respect to wave vectors (reciprocal), in the presence of space-inversion symmetry.

However, with broken space-inversion symmetry, the operators are no longer the same in Eqs. (A3) and (A5). Therefore, $\omega_{n\mathbf{k}} \neq \omega_{n-\mathbf{k}}$. In other words, frequencies are not symmetric with respect to wave vectors (nonreciprocal) when both time-reversal and space-inversion symmetries are broken.

[1] S. John, Phys. Rev. Lett. **58**, 2486 (1987).
[2] E. Yablonovitch, Phys. Rev. Lett. **58**, 2059 (1987).
[3] S. John, Phys. Rev. Lett. **53**, 2169 (1984).
[4] A. Chutinan and S. Noda, Appl. Phys. Lett. **75**, 3739 (1999).
[5] A. Chutinan, S. John, and O. Toader, Phys. Rev. Lett. **90**, 123901 (2003).
[6] A. Chutinan and S. John, Phys. Rev. E **71**, 026605 (2005).
[7] A. Mekis, J. C. Chen, I. Kurland, S. Fan, P. R. Villeneuve, and J. D. Joannopoulos, Phys. Rev. Lett. **77**, 3787 (1996).
[8] A. Mekis, S. Fan, and J. D. Joannopoulos, Phys. Rev. B **58**, 4809 (1998).
[9] M. M. Sigalas, R. Biswas, K. M. Ho, C. M. Soukoulis, D. Turner, B. Vasiliu, S. C. Kothari, and S. Lin, Microwave Opt. Technol. Lett. **23**, 56 (1999).
[10] S. Fan, P. R. Villeneuve, J. D. Joannopoulos, and H. A. Haus, Phys. Rev. Lett. **80**, 960 (1998).
[11] T. Asano, B. S. Song, Y. Tanaka, and S. Noda, Appl. Phys. Lett. **83**, 407 (2003).
[12] G. Brooker, *Modern Classical Optics* (Oxford University Press, Oxford, 2003).
[13] A. F. Popkov, M. Fehndrich, O. Zhuromskyy, and H. Dötsch, J. Appl. Phys. **84**, 3020 (1998).
[14] J. Fujita, M. Levy, R. M. Osgood, Jr., L. Wilkens, and H. Dötsch, Appl. Phys. Lett. **76**, 2158 (2000).
[15] L. Wilkens, D. Träger, H. Dötsch, A. F. Popkov, and A. M. Alekseev, Appl. Phys. Lett. **79**, 4292 (2001).
[16] J. Fujita, M. Levy, R. U. Ahmad, R. M. Osgood, Jr., M. Randles, C. Gutierrez, and R. Villareal, Appl. Phys. Lett. **75**, 998 (1999).
[17] J. Fujita, M. Levy, R. M. Osgood, Jr., L. Wilkens, and H. Dötsch, Appl. Phys. Lett. **76**, 2158 (2000).
[18] N. Kono and Y. Tsuji, J. Lightwave Technol. **22**, 1741 (2004).
[19] Z. Wang and S. Fan, Opt. Express **30**, 1989 (2005).
[20] Z. Wang and S. Fan, Appl. Phys. B: Lasers Opt. **81**, 369 (2005).
[21] S. D. Sarma, A. Pinczuk, and S. D. Sarma, *Perspectives in Quantum Hall Effects: Novel Quantum Liquids in Low-Dimensional Semiconductor Structures* (Wiley-Interscience, New York, 1996).
[22] F. D. M. Haldane and S. Raghu, Phys. Rev. Lett. **100**, 013904 (2008).
[23] S. Raghu and F. D. M. Haldane, e-print arXiv:cond-mat/0602501v3.
[24] H. Takeda and S. John (unpublished).
[25] A. Figotin and I. Vitebsky, Phys. Rev. E **63**, 066609 (2001).
[26] W. V. Parys, B. Moeyersoon, D. V. Thourhout, R. Baets, M. Vanwolleghem, B. Dagens, J. Decobert, O. L. Gouezigou, D. Make, R. Vanheertum, and L. Lagae, Appl. Phys. Lett. **88**, 071115 (2006).
[27] K. M. Ho, C. T. Chan, and C. M. Soukoulis, Phys. Rev. Lett. **65**, 3152 (1990).
[28] K. Busch and S. John, Phys. Rev. E **58**, 3896 (1998).
[29] A. Taflove and S. C. Hagness, *Computational Electrodynamics: The Finite-Difference Time-Domain Method* (Artech House, Boston, 1995).
[30] K. Busch, S. F. Mingaleev, A. Garcia-Martin, M. Schillinger, and D. Hermann, J. Phys.: Condens. Matter **15**, R1233 (2003).
[31] H. Takeda, A. Chutinan, and S. John, Europhys. Lett. **76**, 222 (2006).
[32] H. Takeda, A. Chutinan, and S. John, Phys. Rev. B **74**, 195116 (2006).
[33] N. Adachi, V. P. Denysenkov, S. I. Khartsev, A. M. Grishin, and T. Okuda, J. Appl. Phys. **88**, 2734 (2000).
[34] W. E. Hagston, T. Stirner, and J. Miao, Phys. Rev. B **59**, 5784

(1999).
[35] J. Sinova, T. Jungwirth, J. Kucera, and A. H. MacDonald, Phys. Rev. B **67**, 235203 (2003).
[36] R. Vidya, P. Ravindran, A. Kjekshus, and H. Fjellvag, Phys. Rev. B **70**, 184414 (2004).
[37] C. Chen, X. Wang, A. Liu, and H. Wu, J. Appl. Phys. **87**, 6463 (2000).
[38] K. Ando, H. Saito, Z. Jin, T. Fukumura, M. Kawasaki, Y. Matsumoto, and H. Koinuma, Appl. Phys. Lett. **78**, 2700 (2001).
[39] M. Osada, Y. Ebina, K. Takada, and T. Sasaki, Adv. Mater. (Weinheim, Ger.) **18**, 295 (2006).
[40] J. O. Dimmock, C. E. Hurwitz, and T. B. Reed, Appl. Phys. Lett. **14**, 49 (1969).
[41] J. O. Dimmock, IBM J. Res. Dev. **14**, 301 (1970).
[42] P. Wachter, Phys. Kondens. Mater. **8**, 80 (1968).
[43] J. R. Goldman, T. D. Ladd, F. Yamaguchi, and Y. Yamamoto, Appl. Phys. A: Mater. Sci. Process. **71**, 11 (2000).
[44] A. Chutinan and S. John, Phys. Rev. B **72**, 161316(R) (2005).
[45] A. Chutinan and S. John, Opt. Express **14**, 1266 (2006).